

Development of a hybrid molecular beam epitaxy deposition system for in situ surface x-ray studies

Tassie K. Andersen, Seyoung Cook, Erika Benda, Hawoong Hong, Laurence D. Marks, and Dillon D. Fong

Citation: *Review of Scientific Instruments* **89**, 033905 (2018); doi: 10.1063/1.5008369

View online: <https://doi.org/10.1063/1.5008369>

View Table of Contents: <http://aip.scitation.org/toc/rsi/89/3>

Published by the [American Institute of Physics](#)

Articles you may be interested in

[A general approach to obtain soft x-ray transparency for thin films grown on bulk substrates](#)

Review of Scientific Instruments **88**, 103701 (2017); 10.1063/1.5006522

[Nanometer-resolution depth-resolved measurement of fluorescence-yield soft x-ray absorption spectroscopy for FeCo thin film](#)

Review of Scientific Instruments **88**, 083901 (2017); 10.1063/1.4986146

[Unraveling interfacial strain and interfacial lattice reconstruction mechanism of ultrathin \$\text{LaMnO}_{3+\delta}\$ layers in \$\text{LaMnO}_{3+\delta}/\text{SrTiO}_3\$ superlattices](#)

Journal of Applied Physics **122**, 085309 (2017); 10.1063/1.4998958

[Structural and electrical properties of single crystalline \$\text{SrZrO}_3\$ epitaxially grown on Ge \(001\)](#)

Journal of Applied Physics **122**, 084102 (2017); 10.1063/1.5000142

[X-ray spectrometer having 12 000 resolving power at 8 keV energy](#)

Review of Scientific Instruments **88**, 103107 (2017); 10.1063/1.4999995

[In-situ synchrotron x-ray studies of the microstructure and stability of \$\text{In}_2\text{O}_3\$ epitaxial films](#)

Applied Physics Letters **111**, 161602 (2017); 10.1063/1.4997773



Development of a hybrid molecular beam epitaxy deposition system for *in situ* surface x-ray studies

Tassie K. Andersen,^{1,2} Seyoung Cook,^{1,2} Erika Benda,³ Hawoong Hong,³ Laurence D. Marks,² and Dillon D. Fong¹

¹Materials Science Division, Argonne National Laboratory, 9700 S. Cass Ave., Argonne, Illinois 60439, USA

²Department of Materials Science and Engineering, Northwestern University, 2220 Campus Dr., Evanston, Illinois 60208, USA

³Advanced Photon Source, Argonne National Laboratory, 9700 S. Cass Ave., Argonne, Illinois 60439, USA

(Received 5 October 2017; accepted 17 February 2018; published online 8 March 2018)

A portable metalorganic gas delivery system designed and constructed to interface with an existing molecular beam epitaxy chamber at beamline 33-ID-E of the Advanced Photon Source is described. This system offers the ability to perform *in situ* X-ray measurements of complex oxide growth via hybrid molecular beam epitaxy. The performance of the hybrid molecular beam epitaxy system while delivering metalorganic source materials is described. The high-energy X-ray scattering capabilities of the hybrid molecular beam epitaxy system are demonstrated both on oxide films grown solely from the metalorganic source and ABO₃ oxide perovskites containing elements from both the metalorganic source and a traditional effusion cell. *Published by AIP Publishing.* <https://doi.org/10.1063/1.5008369>

I. INTRODUCTION

As the applications for oxide materials grow more diverse to include gas sensing,¹ solid oxide fuel cells,^{2,3} electrochemical supercapacitors,⁴ solar cells,^{5,6} catalysis,^{7,8} and resistive switching⁹ so do the range of desirable material properties. To address this need, fabrication methods combining a high degree of precision with the possibility for industrial scale-up are a necessity to bring next-generation oxide-based devices to market. One promising oxide film synthesis method, utilizing a combination of metalorganic and solid metal sources, is hybrid molecular beam epitaxy (HMBE).

Film deposition systems employing metalorganic precursors in ultra-high vacuum (UHV) conditions have been in use since the 1980s,^{10–13} with synthesis initially focused on III/V semiconductors but later expanded to include oxides such as the high T_c-superconductor, yttrium barium copper oxide.¹⁴ Of late, there has been renewed interest in HMBE for growth of an increasingly wide range of oxide materials.^{15–18} This is due to the fact that HMBE has multiple advantages over conventional molecular beam epitaxy (MBE) for oxide synthesis. Metalorganic precursors offer the same elements available as solid metal sources in MBE, but permit the delivery of cations that would otherwise require prohibitively high source temperatures. Additionally, HMBE does not rely on the extreme deposition conditions created by the introduction of ozone or an oxygen plasma to maintain stoichiometry,^{19–21} as many metalorganic compounds contain the necessary oxygen in their ligand functionality.²² This avoids the significant risk in MBE of oxidizing the metal sources themselves that would lead to diminished efficiency and stoichiometric control.^{23,24}

Advances in oxide film synthesis necessitate the development of the proper characterization tools to understand the complex behavior associated with these multicomponent materials. *In situ* X-ray scattering utilizing the brilliance of synchrotron X-ray sources offers opportunities to probe film

synthesis at the atomic scale.^{25–27} In particular, surface X-ray diffraction (SXRD) allows the use of many surface-sensitive methods well-suited to the investigation of thin film growth. These techniques include grazing incidence X-ray scattering and spectroscopy,²⁸ measurement of crystal truncation rods (CTRs) and fractional-order peaks, and diffuse scattering, all of which can be applied to films comprised of only a few atomic layers. Exploiting these techniques reveals the structure on multiple length scales from defects, surface reconstructions, island sizes and distributions to domains, while the *in situ* capabilities allow the evolution of these features to be observed.

We describe here the design and testing of an HMBE metalorganic delivery system for use with an *in situ* surface x-ray diffraction (SXRD) MBE setup at Sector 33-IDE of the Advanced Photon Source (APS). *In situ* SXRD permits detailed studies of the growth mechanisms involved in HMBE, allowing comparison to other synthesis methods. As HMBE systems are uncommon and the only prior *in situ* data came from reflection high-energy electron diffraction (RHEED) studies,^{29,30} this unique instrument provides new insight into this powerful synthesis technique and the atomic-scale processes that take place during the growth of complex oxide thin films.

II. DESCRIPTION OF INSTRUMENT

A. System design

The design goals for the HMBE gas delivery system were to implement two lines for different metalorganics that were compact and mobile and could easily be integrated into existing chambers.

The precursor piping was designed to interface with an existing oxide MBE chamber located at APS Sector 33-IDE. The oxide MBE chamber and six-circle diffractometer are shown in Fig. 1 with the axes of motion required

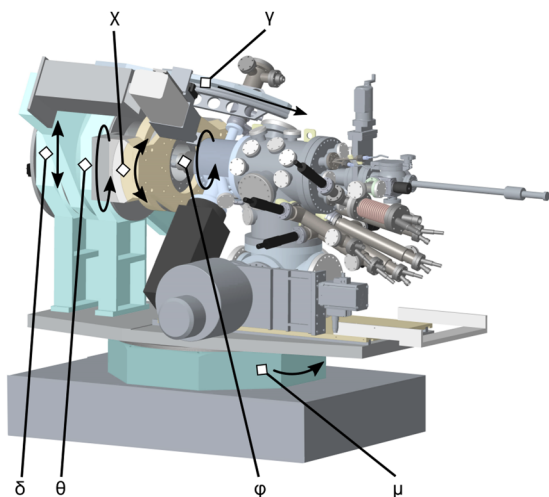


FIG. 1. Schematic depiction of the *in situ* X-ray system for hybrid MBE growth. The oxide MBE chamber is mounted on a six-circle diffractometer with the axes of motion indicated.³¹

to satisfy a range of diffraction conditions necessary for *in situ* SXRDL labeled.^{31,32} This growth chamber has a roughing pump and 1000 l/s turbo pump, which provide a base chamber pressure in the 10^{-9} Torr range. Much of the equipment associated with the HMBE is mounted on a mobile, vertical rack (Fig. 2) that is rigidly attached to the diffractometer to accommodate the movement of the experimental setup.

To avoid strain on the stage motors, the vertically oriented rack is constructed from a lightweight 80/20 T-slotted aluminum frame. The frame allows the gas piping, valves, meters, and controllers to be permanently attached and organized for ease of use. The rack supports a dedicated scroll pump (Edwards Vacuum, UK) [Fig. 2(G)] with a peak pump speed of $6.2 \text{ m}^3/\text{h}$, able to achieve an ultimate vacuum of 0.015 Torr, used to evacuate lines and serve as an exhaust. Two precursor gas sources are contained in a stainless-steel gas enclosure (Applied Energy Systems, USA) [Fig. 2(J)] designed with adequate exhaust ventilation for safe use with hazardous and flammable gases [Fig. 2(L)]. Gas piping and bellows-sealed valves (Swagelok, USA) [Figs. 2(A), 2(F), and 2(I)] for rapid on/off line switching are attached to and supported by the aluminum frame. These valves are controlled by a bank of solenoids [Fig. 2(E)] mounted to the rack and a digital data acquisition I/O device (National Instruments, USA) [Fig. 2(D)] for remote computer communication. Each line utilizes a metal-sealed control valve with a stepper motor (MKS Instruments, USA) [Fig. 2(K)] (hereafter referred to as a mechanical leak valve) and pressure capacitance manometer (MKS Instruments, USA) [Fig. 2(H)] with a range of 1 Torr, located at the top. The self-tuning/digital proportional-integral-derivative (PID) pressure controllers (MKS Instruments, USA) [Fig. 2(C)] for this valve/pressure capacitance manometer combination are mounted opposite the mechanical leak valves near the top of the frame. Additional autotuned PID/on-off controllers (Omega Engineering, USA) [Fig. 2(B)] for heating are mounted directly above and below the mechanical leak valve controllers. The placement of all controllers was

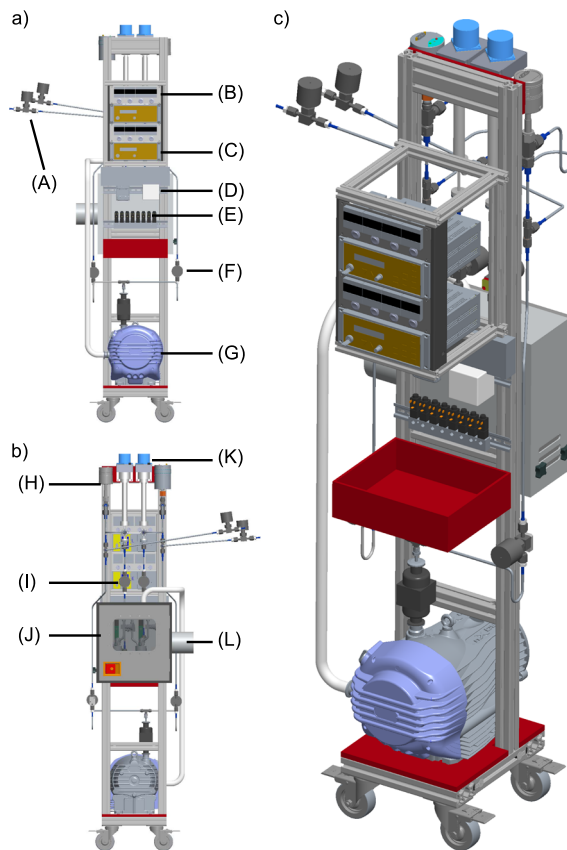


FIG. 2. Schematic of the mobile, vertical rack for the *in situ* hybrid MBE chamber. Views from the front (a), the back (b), and at angle (c) with the labeled components described in the text. Labeled parts are bellows-sealed pneumatic valves (A), (F), and (I), heating controllers (B), line pressure/mechanical valve controller (C), digital I/O for pneumatic valves (D), pneumatic valve solenoids (E), scroll pump (G), pressure capacitance manometer (H), source enclosure (J), metal-sealed mechanical stepper valve (K), and exhaust vent hookup (L).

chosen such that the displays are located near eye level. A power strip and shelf for convenient storage of miscellaneous tools and materials are located near the center of the rack.

As shown in Fig. 2, components are mounted on both sides of the aluminum rack to balance weight. Heavier components, including the pump and source enclosure, are located nearer to the floor to prevent instability during motion. The rack is fixed with an arm rigidly attached to the stage base as shown in Fig. 3 (arm in green) in order to follow the rotary motion of the μ -axis (Fig. 1) during X-ray measurements. Additionally, the wheeled base provides portability between multiple experimental setups, as necessary. Figure 3 shows the deposition system in its in-use configuration, highlighting the compact, self-contained assembly and small footprint. The gas piping meets the UHV chamber at a custom showerhead dual injector (Riber, USA) ensuring that both gas inlets, located near the same position, are heated independently. This injector was installed with a conflat flange normally reserved for effusion cells on the MBE chamber. The piping is fully modular, with VCR[®] metal gasket face seal fittings (Swagelok, USA). The final length of line between the rack and MBE can be replaced to accommodate deposition chambers of different geometries.

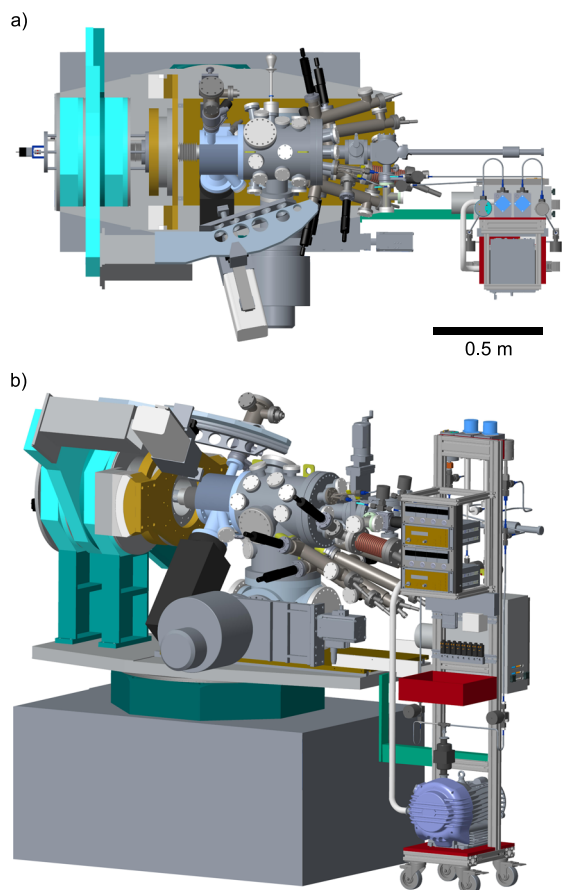


FIG. 3. Schematic of the entire *in situ* hybrid MBE system, showing the placement and attachment of the vertical rack used to deliver the metalorganic precursors, relative to the oxide MBE chamber and six-circle diffractometer, as viewed from the top (a) and side (b).

B. Gas handling

The gas handling system was designed for the simultaneous or independent delivery of two metalorganic precursors. The gas flux from each source is maintained through regulation of the delivery line pressure and can be directed either to the deposition chamber or to a self-contained pump and exhaust vent, via pneumatic valves and a mechanical leak valve coupled with a control loop. A diagram of the delivery system is shown in Fig. 4.

The source bottles contain metalorganic precursors, here compounds constituting the B-site cation in the perovskite structure, ABO_3 , such as titanium(IV) isopropoxide (TTIP) and vanadium(V) oxytriisopropoxide (VTIP). No carrier gas is employed, and the rate of delivery is dependent on the source vapor pressure and temperature. The gas flux is controlled using a feedback/control loop where a pressure capacitance manometer provides feedback to a PID controller that drives the position of a mechanical leak valve. In this manner, a steady vapor flux is achieved. The background pressure of the MBE chamber, in the 10^{-9} Torr range, is increased to 1×10^{-6} Torr by addition of either O_2 or O_3 as needed for oxide growth. The metalorganic is then delivered, bringing the typical chamber pressure to the $1\text{--}2 \times 10^{-5}$ Torr range. For these pressures, the MBE chamber's roughing and turbo pumps are sufficient.

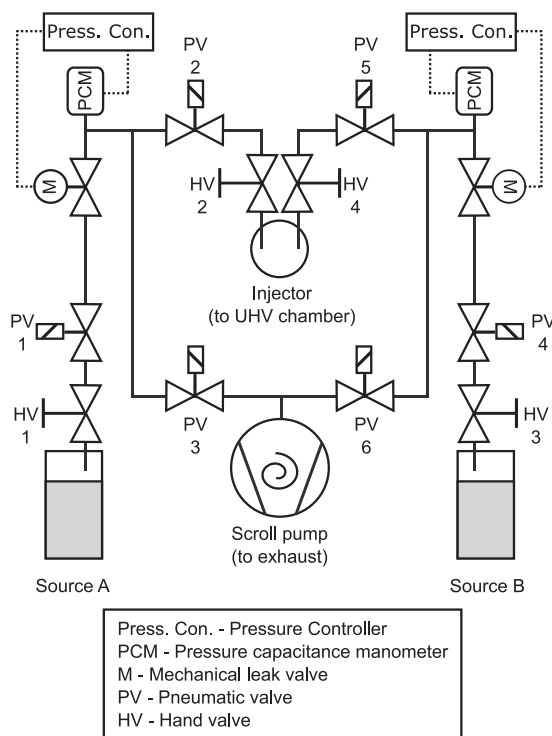


FIG. 4. Diagram of the hybrid MBE gas delivery system, indicating the placement of the valves and pressure controllers.

Each line has an independent feedback/control loop so that deposition from two sources at different flux rates is possible either concurrently or while being switched independently. Switching of sources proceeds as follows: while source A enters the chamber, source B is directed to an exhaust vent via the pump mounted at the cart's base; when the sources are switched, their destinations are exchanged. A constant gas flow is maintained from the source to either the chamber or exhaust while switching to minimize pressure fluctuations. The line in the exhaust is evacuated using the scroll pump by way of a particulate filter. Furthermore, the exhaust from the pump is redirected to the source bottle enclosure, where the gases are then removed via a side vent integrated into the hazardous gas ventilation system at the beamline 33-ID. The valves controlling the switches also serve to isolate different sections of piping during system modifications, bake-out, and leak checking. Two hand valves are present: one downstream of the source bottle for quick replacement and one directly upstream of the chamber injector to improve ease of installation.

The source bottles are heated to ensure sufficient vapor pressures for film growth, as shown by the single-line schematic in Fig. 5. The lines are heated in four zones: source bottle (zone A), delivery and vent line (zones B and C), and injector (zone D). The temperature (T) of each zone increases from the source to the injector/exhaust such that $T_{\text{zone A}} < T_{\text{zone B}} < T_{\text{zone C}} < T_{\text{zone D}}$. The exact temperature of each zone is chosen to provide sufficient vapor pressure for remaining within the mechanical leak valve and controller operating limits while avoiding condensation or metalorganic decomposition at the temperature extremes. For a TTIP source, the bottle, $T_{\text{zone A}}$, is kept at 72°C , $T_{\text{zone B}}$ piping at 85°C , $T_{\text{zone C}}$ at 95°C , and the MBE chamber injector,

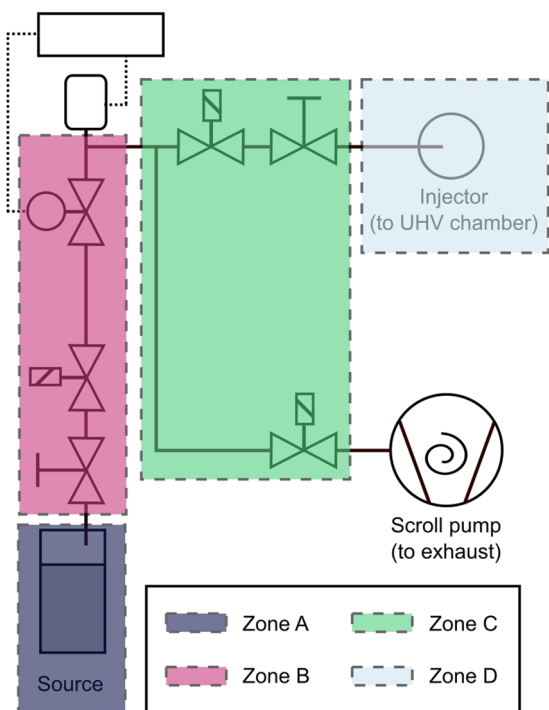


FIG. 5. Diagram illustrating the different temperature zones for a single hybrid MBE gas delivery line. Labels of the different valves and pressure controllers are shown in Fig. 4.

$T_{\text{zone D}}$, at 115 °C. This provides a calculated vapor pressure $P_{\text{eq,TTIP}} = 3836.4 \text{ mTorr}$ ($5.0479 \times 10^{-3} \text{ atm}$)³³ in the source headspace.

Each zone has a dedicated PID temperature controller. Controllers are set up to regulate the zone temperature such that, once heated, temperatures are stable to within ± 0.5 °C. To ensure even heating of the lines, they are wrapped uniformly with a heating tape within a given zone and insulated with layers of aluminum foil. On one individual dosing line, there is an internally heated pressure capacitance manometer (MKS Instruments, USA) with a working temperature of 200 °C to prevent condensation for use with sources requiring higher temperatures than the standard acceptable operating range of 50 °C.

There are safety guidelines to follow when using this system. During deposition operation, the system is hot and care should be taken to wear insulated gloves when operating any hand valves. All interaction with sources should be performed while an exhaust system is running, to ensure constant flow of any potentially hazardous material away from the experimenter. Installation and removal of sources may be performed if the source and piping are at room temperature. Before changing the source, the bubbler should be isolated by closing the hand valve. Piping should be evacuated via the vent system that is attached to the experiment area's exhaust handling (scroll pump on the gas delivery cart) to avoid buildup of excess pressure. A positive nitrogen flow to preserve air-sensitive source materials can be provided if necessary through the vented MBE chamber. If this is not possible, the valve directly downstream of the source should be closed. Proper personal protective equipment for the specific gas hazards of the source must be utilized. Once the source has been removed, the VCR[®] fittings

should be examined to determine whether any oxidation or corrosion has occurred requiring replacement of parts.

Source installation follows this process in reverse. Either a positive nitrogen flow should be present or all valves closed. After installation of the source, the system piping should be evacuated via the exhaust system before opening the bubbler hand valve. Once the source valve is open, the source and lines should be heated to the desired temperature, keeping the vent on to prevent excess pressure buildup. Once the source is at the desired temperature, the mechanical leak valve may be closed and the exhaust closed in preparation for normal operation.

C. Remote controls

Remote monitoring and control of the HMBE system during growth and *in situ* measurements are made possible through interfaced computers. The programmable pressure controller for the mechanical leak valve and the pressure capacitance manometer feedback/control loop are controlled by the software built on Experimental Physics and Industrial Control System (EPICS),³⁴ where the gas delivery and PID conditions are set on a dedicated graphic user interface (GUI). The pressure controller works by providing inputs to either the direct valve position or the line pressure (where the feedback loop is utilized). Multiple setpoints may be specified with different PID settings. The EPICS software is also used to control the diffractometer and chamber motions, as shown in Fig. 1. Both systems are controlled with the same EPICS interface.

The pneumatic on/off valves are controlled remotely via Laboratory Virtual Instrument Engineering Workbench (LabVIEW[™]) software.³⁵ Two GUIs were written in LabVIEW: one for individual on/off control of each valve and another where pre-written valve schemes can be selected. Pre-written valve schemes are used for the quick termination of sources, switching between sources, and the pump-down actions of different line sections during installation or bake-out. The flexibility in control over the pneumatic valves ensures that the EPICS and LabVIEW operated pressure controllers and valves work in tandem for a variety of actions.

III. SYSTEM PERFORMANCE

A. Gas delivery and rate stability

Functioning of the gas delivery piping and controls were verified with a residual gas analyzer (RGA) (Stanford Research Systems, USA)/mass spectrometer to determine the quantity of the precursor material in the chamber during operation. Initial HMBE testing was conducted using the TTIP source. To verify effective delivery to the substrate position, an RGA was installed at a distance out of sight from the gas injector similar to that of a growth substrate. The mass spectrum collected while the TTIP source was delivered at a chamber pressure of 1×10^{-5} Torr is shown in Fig. 6. The peak at a mass-to-charge ratio (m/z) = 45 corresponding to $[\text{CH}_3\text{CHOH}]^+$,^{36,37} reported as a metalorganic cracking product for TiO_2 growth with TTIP and titanium tetrachloride,³⁶ proved to be ambiguous as an indicator perhaps due to additional hydrocarbons present in the source bubbler. The lowest m/z cracking products of TTIP containing Ti were $[\text{TiO}]^+$ at $m/z = 64$ and $[\text{TiO}(\text{OH})]^+$ at

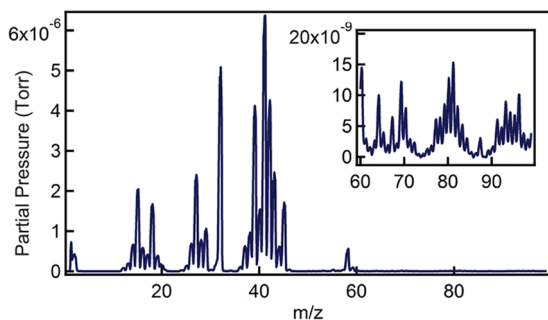


FIG. 6. Partial pressures from cracking products of the TTIP metalorganic as a function of m/z . The measurement was performed during deposition of TiO_2 on r -plane Al_2O_3 in the oxide MBE chamber. The inset shows an enlarged view of the higher m/z products.

$m/z = 81$,³⁷ of which the $m/z = 81$ peak was the more intense, as shown in Fig. 6 inset. This signal was chosen as an indicator for TTIP, as films containing Ti could be grown consistently every time this peak was observed in the RGA spectrum.

Once the presence of TTIP was verified, its behavior during the initiation and termination of delivery was investigated. Furthermore, the stability of the TTIP flux over time periods typical for growth was measured within the same experiment. Time-dependent RGA measurements of the cracking products of TTIP were initiated prior to opening the TTIP line. The mechanical leak valve was then opened to a fixed pressure setpoint using the controller, and the delivery of TTIP was tracked for approximately 30 min before the leak valve was closed. The RGA continued to measure the partial pressures of the chosen cracking products for an additional few minutes. The results of these measurements are summarized in Fig. 7, where the traces of different m/z cracking products are shown in different panels to improve visualization of all the cracking products tracked.

In Fig. 7, before the leak valve is opened, no significant levels of cracking products from TTIP are present. It was also verified that the HMBE lines have no leaks within the RGA detection limit when the valves are closed. When the TTIP valve is switched open (at 660 s in Fig. 7), the increase in all cracking products is abrupt and immediate. In the initial ~ 100 s after opening, there is an increase in the partial pressure of the cracking products to 80%–98% of their stable level, depending on the component. This initial swift increase in the amount of TTIP is followed by a more gradual one for as much as ~ 450 s before reaching saturation. The TTIP partial pressure in the chamber is stable after this point until the mechanical leak valve is closed, approximately 2000 s after delivery began (at 2600 s in Fig. 7), indicating reliable flux stability for time periods on the scale of growth. At this point, the delivery of sources is terminated quickly as the amount of TTIP drops immediately and is equivalent to the initial baseline after only ~ 120 – 180 s. All tracked cracking products of TTIP behave in a similar fashion, indicating no unexpected flux deviations over the time period measured.

B. Growth of TiO_2 on r -plane Al_2O_3

Once TTIP delivery was confirmed and characterized, the HMBE system was utilized to grow a simple binary oxide,

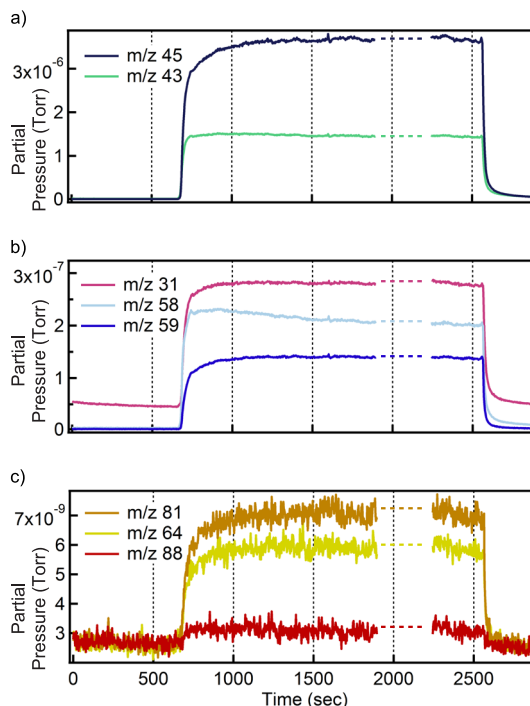


FIG. 7. Partial pressure traces of selected m/z cracking products of the metalorganic precursor, TTIP, during growth of rutile TiO_2 . The RGA measurements show the behavior of precursor gases within the MBE chamber upon initiating and after terminating gas delivery. The traces in (a)–(c) have been re-scaled for ease of viewing. Dotted lines between traces serve as a guide to the eye; no data were recorded during this time. Measurements were taken during growth at a temperature of 800°C .

TiO_2 , on r -plane sapphire, Al_2O_3 (0 1 2), substrates (CrysTec, GmbH). As growth of this material requires only the TTIP metalorganic, it was chosen to demonstrate a simple test case for HMBE. All X-ray diffraction data presented in Secs. III B and III C were acquired at APS Sector 33-IDE, using 15 keV energy X-rays selected by a Si (1 1 1) monochromator. The range of energies selected by this type of monochromator is very narrow. While X-ray effects may arise with highly focused X-rays,³⁸ or non-monochromatic X-rays, we and others have not observed any effect of monochromatic X-rays on growth behavior using metal-organic precursors.^{39–45}

Plots of the specular out-of-plane scattering for two TiO_2 films and real-time diffraction data measured under two different diffraction conditions are shown in Fig. 8. The scan in Fig. 8(a) is shown as a function of reciprocal lattice units (r.l.u.'s), referenced to the (0 1 2) crystallographic room temperature d-spacing of Al_2O_3 , 0.174 nm. Both films show only rutile phase TiO_2 with the orientation $(1\ 0\ 1)\ [0\ 1\ 0]_{\text{TiO}_2} \parallel (0\ 1\ 2)\ [0\ 0\ 1]_{\text{Al}_2\text{O}_3}$ according to Fig. 8(a). The films labeled $\text{TiO}_2\text{h1}$ and $\text{TiO}_2\text{h2}$ were grown consecutively with a line pressure of 75 mTorr TTIP and 50 mTorr, respectively, using a substrate temperature of 600°C . During the deposition of $\text{TiO}_2\text{h1}$, the H K L = 0 0 $\frac{1}{2}$ position along the specular crystal truncation rod (CTR) was monitored [Fig. 8(b)]. The intensity at this anti-Bragg position is extremely sensitive to the growth of epitaxial layers as well as to surface roughness, and the results can easily be compared to previous RHEED studies.²² The second film grown, labeled $\text{TiO}_2\text{h2}$ in Fig. 8(a), was monitored *in situ* at H K L = 0 0 1.42, i.e., at the TiO_2 (1 0 1) Bragg

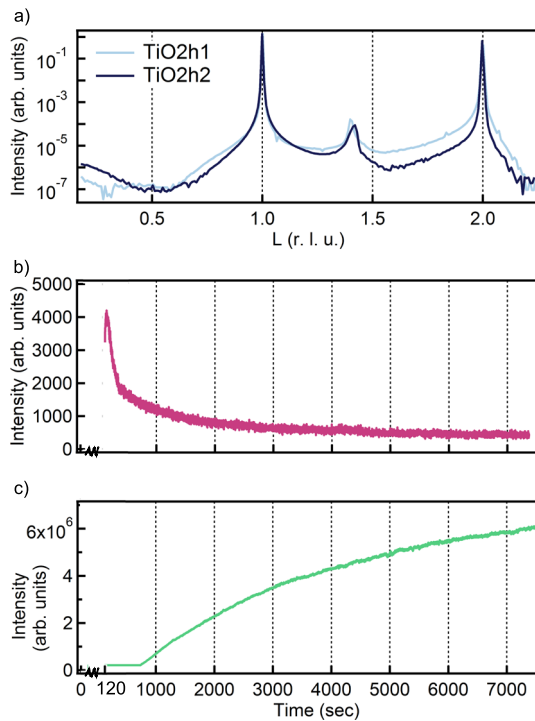


FIG. 8. Scattered X-ray intensities measured (a) along the out-of-plane, $00L$ direction for a rutile TiO_2 film grown on Al_2O_3 (012), (b) at the anti-Bragg position, $HKL = 00\frac{1}{2}$ r.l.u., and (c) at the TiO_2 (101) Bragg peak or $HKL = 001.42$ r.l.u. The measurements were taken at the growth temperature of 600°C . Delivery of TTIP began at $t = 0$; measurement began at $t = 120$ s.

peak [Fig. 8(c)], to monitor its evolution as a function of film thickness. The thickness of each sample, calculated based on Scherrer's equation and the full-width half-maximum of the TiO_2 film peak, was 40 nm for sample TiO2h1 and 24 nm for sample TiO2h2.

These experiments show that the HMBE chamber works in conjunction with the *in situ* SXR D capabilities to investigate the various processes that occur during oxide thin film growth. The measured diffraction conditions can be compared with typical RHEED monitoring.⁴⁶ However, the kinematic, single scattering approximation valid for SXR D facilitates quantitative interpretation of the multiple length scale diffraction results, including those regarding film morphology and evolution. It is also possible to monitor specific diffraction conditions with high precision that are challenging or impossible to track with RHEED due to differences in the scattering behavior and geometry, as shown in Fig. 8(c) for the TiO_2 (101) Bragg peak.

C. Growth of SrTiO_3 on LSAT (001)

Many technologically relevant oxide materials are members or derivatives of the perovskite, ABO_3 , family. To grow these materials, the metalorganic source can be used in conjunction with elemental sources in effusion cells to expand the number of available A and B site cations. We demonstrate this ability through the growth of SrTiO_3 , which was chosen for its structural flexibility as well as the abundance of information available on its properties and phases.

SrTiO_3 was grown on lanthanum aluminate-strontium aluminum tantalite (LSAT) (001) substrates (CrysTec GmbH).

The TTIP precursor was used in combination with a solid metal Sr source supplied via an effusion cell. Plots of the specular CTRs, time-resolved scattering at the anti-Bragg position during growth, and atomic force microscopy (AFM) images of two such films (STOh1 and STOh2) are shown in Figs. 9(a)–9(d), respectively. Here, the reciprocal lattice units are referenced to the room temperature lattice constant of LSAT (001), 0.387 nm. Both of the SrTiO_3 films grown on LSAT were observed to have the orientation $(001)[001]_{\text{SrTiO}_3} \parallel (001)[001]_{\text{LSAT}}$. The samples were grown under near-identical conditions at a substrate temperature of 750°C with 110 mTorr of TTIP line pressure. The Sr flux for sample STOh1 was 2.35×10^{12} atoms/ cm^2 s, while Sr flux for STOh2 was of 2.67×10^{12} atoms/ cm^2 s, as calibrated by a quartz crystal microbalance. From the film peak position near the (001) substrate Bragg peak, the c -lattice parameters of STOh1 and STOh2 were 0.401 nm and 0.395 nm at room temperature, indicating that STOh2 had better stoichiometry, based on the ideal c -lattice parameter of coherently strained SrTiO_3 on LSAT (0.393 nm, assuming a bulk-like Poisson's ratio of $\nu = 0.23$). The root-mean-squared roughness of STOh1 and STOh2 was 0.28 and 0.15 nm, respectively, while their thicknesses, calculated from the thickness fringes in Fig. 9(a), were 10.9 and 7.5 nm, respectively. Unit cell steps and terraces are visible in Fig. 9(d),

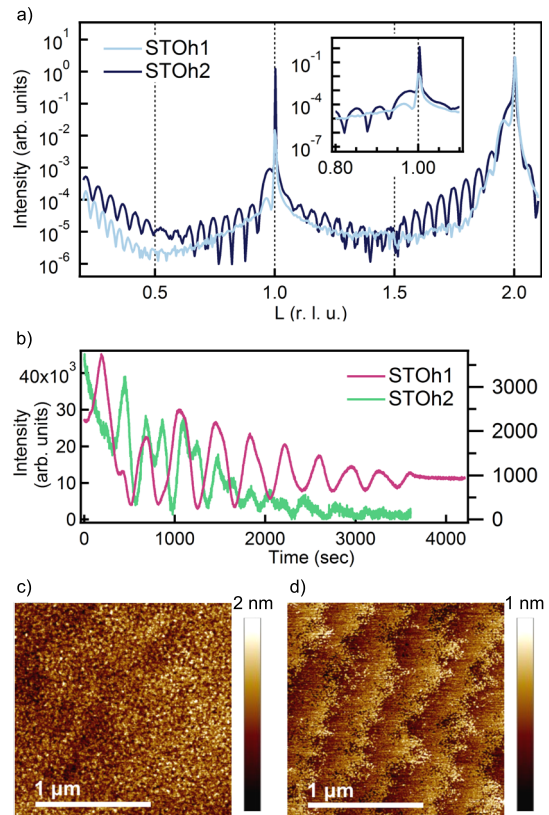


FIG. 9. Room temperature results for two SrTiO_3 films grown at 750°C on LSAT (001) with 110 mTorr TTIP under Sr fluxes of 2.35×10^{12} atoms/ cm^2 s (STOh1) and 2.67×10^{12} atoms/ cm^2 s (STOh2). (a) X-ray scattering along the specular $00L$ direction at room temperature. (b) Scattered X-ray intensities measured during growth at 750°C at the reciprocal lattice position, $HKL = 00\frac{1}{2}$ r.l.u. [(c) and (d)] Room temperature $2 \mu\text{m} \times 2 \mu\text{m}$ AFM micrographs of the films STOh1 (c) and STOh2 (d).

indicating that high quality surfaces can be achieved under the proper growth conditions.

Our system supports the use of a wide range of metalorganic precursors and solid metal sources, permitting *in situ* studies of many different complex oxides. We expect that this unique instrument will provide much needed insight into synthesis of these multifunctional materials.

IV. DISCUSSION AND OUTLOOK

As the high-quality synthesis of an increasingly wide variety of oxide materials becomes necessary, so does the development of instrumentation able to probe *in situ* the many disparate growth processes. Hybrid MBE is a powerful growth technique able to access a wider variety of metal cations as compared to MBE; furthermore, the HMBE method facilitates more rapid synthesis of complex oxide films, often with fewer compositional defects. The hybrid MBE instrument described here is interfaced directly with a surface X-ray diffractometer to permit *in situ* experiments aimed at gaining a deeper understanding of the atomic scale mechanisms that take place during oxide crystal growth.

Our results demonstrate the power of *in situ* X-ray scattering for HMBE growth studies. We observed an initial change in the precursor flux (Fig. 7), but this did not appear to have any detrimental effect on the quality of films produced, even when coupling disparate sources to grow SrTiO₃. Strategies for combating the initial change in pressure upon opening the metalorganic valve rely on venting the gas being delivered, via the exhaust pump piping utilizing the cart pump mounted on the aluminum rack. This is performed for a set amount of time to stabilize the gas inlet pressure before switching to delivery to the growth chamber. This is the method outlined in a recent review of HMBE systems and growth by Brahlek *et al.*⁴⁷ As with any deposition system, the growth rate is ultimately limited by the flux of the slowest source, which in the demonstrated case is the solid metal, Sr. For the growth of materials where the appropriate precursors have not yet been identified as replacements for solid metals, the speed advantage that HMBE offers is diminished, making it a less practical choice.

Planned studies exploiting the unique capabilities of this system will focus on understanding oxide thin film growth dynamics. Data from these experiments will be compared to those from *in situ* RHEED measurements, ultimately providing a more complete picture of thin film synthesis and interfacial evolution. These studies will also be used to investigate the potential of hybrid MBE as a method for producing high quality films for next-generation oxide devices. As this hybrid system was designed with portability in mind, it can also be coupled to other existing (and future) film growth setups, such as a pulsed laser deposition system, to provide an alternative source capability.⁴⁸

ACKNOWLEDGMENTS

We would like to thank Dr. Roman Engel-Herbert and Dr. Bharat Jalan for their productive discussions. T.K.A., S.C.,

and D.D.F. were supported by the U.S. Department of Energy (DOE), Office of Science, Office of Basic Energy Sciences, Division of Materials Science and Engineering. This research used resources of the Advanced Photon Source, a DOE Office of Science User Facility operated for the DOE Office of Science by Argonne National Laboratory under Contract No. DE-AC02-06CH11357.

- ¹H.-J. Kim and J.-H. Lee, *Sens. Actuators, B* **192**, 607 (2014).
- ²C. Sun, R. Hui, and J. Roller, *J. Solid State Electrochem.* **14**, 1125 (2010).
- ³E. Wachsman and K. Lee, *Science* **334**, 935 (2011).
- ⁴G. Wang, L. Zhang, and J. Zhang, *Chem. Soc. Rev.* **41**, 797 (2012).
- ⁵I. Grinberg, D. V. West, M. Torres, G. Gou, D. M. Stein, L. Wu, G. Chen, E. M. Gallo, A. R. Akbashev, P. K. Davies, J. E. Spanier, and A. M. Rappe, *Nature* **503**, 509 (2013).
- ⁶J. You, L. Meng, T.-B. Song, T.-F. Guo, Y. Yang, W.-H. Chang, Z. Hong, H. Chen, H. Zhou, Q. Chen, Y. Liu, N. D. Marco, and Y. Yang, *Nat. Nanotechnol.* **11**, 75 (2015).
- ⁷G. Centi and S. Perathoner, *Microporous Mesoporous Mater.* **107**, 3 (2008).
- ⁸J. Suntivich, K. May, H. Gasteiger, J. Goodenough, and Y. Shao-Horn, *Science* **334**, 1383 (2011).
- ⁹A. Sawa, *Mater. Today* **11**, 28 (2008).
- ¹⁰M. Panish, *J. Electrochem. Soc.* **127**, 2729 (1980).
- ¹¹E. Tokumitsu, Y. Kudou, M. Konagai, and K. Takahashi, *J. Appl. Phys.* **55**, 3163 (1984).
- ¹²E. Veuhoff, W. Pletschen, P. Balk, and H. Lüth, *J. Cryst. Growth* **55**, 30 (1981).
- ¹³W. T. Tsang, *J. Cryst. Growth* **111**, 529 (1991).
- ¹⁴K. Endo, S. Saya, S. Misawa, and S. Yoshida, *Thin Solid Films* **206**, 143 (1991).
- ¹⁵H.-T. Zhang, L. Zhang, D. Mukherjee, Y.-X. Zheng, R. C. Haislmaier, N. Alem, and R. Engel-Herbert, *Nat. Commun.* **6**, 8475 (2015).
- ¹⁶B. Jalan, P. Moetakef, and S. Stemmer, *Appl. Phys. Lett.* **95**, 032906 (2009).
- ¹⁷J. M. LeBeau, R. Engel-Herbert, B. Jalan, J. Cagnon, P. Moetakef, S. Stemmer, and G. B. Stephenson, *Appl. Phys. Lett.* **95**, 142905 (2009).
- ¹⁸K. Masaki, H. Isshiki, and T. Kimura, *Opt. Mater.* **27**, 876 (2005).
- ¹⁹D. D. Berkley, B. R. Johnson, N. Anand, K. M. Beauchamp, L. E. Conroy, A. M. Goldman, J. Maps, K. Mauersberger, M. L. Mecartney, J. Morton, M. Tuominen, and Y. J. Zhang, *Appl. Phys. Lett.* **53**, 1973 (1988).
- ²⁰D. G. Schlom, A. F. Marshall, J. T. Sizemore, Z. J. Chen, J. N. Eckstein, I. Bozovic, K. E. Von Dessenbeck, J. S. Harris, and J. C. Bravman, *J. Cryst. Growth* **102**, 361 (1990).
- ²¹J. N. Eckstein, D. G. Schlom, E. S. Hellman, K. E. von Dessenbeck, Z. J. Chen, C. Webb, F. Turner, J. S. Harris, Jr., M. R. Beasley, and T. H. Geballe, *J. Vac. Sci. Technol., B* **7**, 319 (1989).
- ²²B. Jalan, R. Engel-Herbert, J. Cagnon, and S. Stemmer, *J. Vac. Sci. Technol., A* **27**, 230 (2009).
- ²³E. S. Hellman and E. H. Hartford, *J. Vac. Sci. Technol., B: Microelectron. Nanometer Struct.–Process., Meas., Phenom.* **12**, 1178 (1994).
- ²⁴C. Kim, H. Chaparro, S. Gross, N. Oh, and N. Bansal, *J. Vac. Sci. Technol., A* **28**, 271 (2010).
- ²⁵Z. Feng, Y.-L. Lee, W. T. Hong, Y. Shao-Horn, Y. Yacoby, H. Zhou, M. D. Biegalski, H. M. Christen, M. J. Gadre, D. Morgan, and S. B. Adler, *J. Phys. Chem. Lett.* **5**, 1027 (2014).
- ²⁶A. Gray, Y. Liu, H. Hong, and T. C. Chiang, *Phys. Rev. B* **87**, 195415 (2013).
- ²⁷M. Holt, M. Sutton, P. Zschack, H. Hong, and T. C. Chiang, *Phys. Rev. Lett.* **98**, 065501 (2007).
- ²⁸P. H. Fuoss and S. Brennan, *Annu. Rev. Mater. Res.* **20**, 365 (1990).
- ²⁹M. Brahlek, L. Zhang, C. Eaton, H.-T. Zhang, and R. Engel-Herbert, *Appl. Phys. Lett.* **107**, 143108 (2015).
- ³⁰H. T. Zhang, L. R. Dedon, L. W. Martin, and R. Engel-Herbert, *Appl. Phys. Lett.* **106**, 233102 (2015).
- ³¹H. Hong and T. C. Chiang, *Nucl. Instrum. Methods Phys. Res., Sect. A* **572**, 942 (2007).
- ³²J. H. Lee, I. C. Tung, S. H. Chang, A. Bhattacharya, D. D. Fong, J. W. Freeland, and H. Hong, *Rev. Sci. Instrum.* **87**, 013901 (2016).
- ³³K. Siefert and G. Griffin, *J. Electrochem. Soc.* **137**, 814 (1990).
- ³⁴See <http://www.aps.anl.gov/epics/> for description of the open source Experimental Physics and Industrial Control System (EPICS).
- ³⁵See www.ni.com/en-us/shop/labview.html for LabVIEW–National Instruments, National Instruments, 2017.

- ³⁶V. R. Anderson, A. S. Cavanagh, A. I. Abdulagatov, Z. M. Gibbs, and S. M. George, *J. Vac. Sci. Technol., A* **32**, 01A114 (2014).
- ³⁷A. Rahtu and M. Ritala, *Chem. Vapor Dep.* **8**, 21 (2002).
- ³⁸S. O. Hruszkewycz, M. Allain, M. V. Holt, C. E. Murray, J. R. Holt, P. H. Fuoss, and V. Chamard, *Nat. Mater.* **16**, 244 (2016).
- ³⁹R. Boichot, L. Tian, M.-I. Richard, A. Crisci, A. Chaker, V. Cantelli, S. Coindeau, S. Lay, T. Ouled, and C. Guichet, *Chem. Mater.* **28**, 592 (2016).
- ⁴⁰D. D. Fong, J. A. Eastman, S. K. Kim, T. T. Fister, M. J. Highland, P. M. Baldo, and P. H. Fuoss, *Appl. Phys. Lett.* **97**, 191904 (2010).
- ⁴¹F. Jiang, A. Munkholm, R.-V. Wang, S. K. Streiffer, C. Thompson, P. H. Fuoss, K. Latifi, K. R. Elder, and G. B. Stephenson, *Phys. Rev. Lett.* **101**, 086102 (2008).
- ⁴²M. V. R. Murty, S. K. Streiffer, G. B. Stephenson, J. A. Eastman, G.-R. Bai, A. Munkholm, O. Auciello, and C. Thompson, *Appl. Phys. Lett.* **80**, 1809 (2002).
- ⁴³M.-I. Richard, M. J. Highland, T. T. Fister, A. Munkholm, J. Mei, S. K. Streiffer, C. Thompson, P. H. Fuoss, and G. B. Stephenson, *Appl. Phys. Lett.* **96**, 051911 (2010).
- ⁴⁴G. B. Stephenson, J. A. Eastman, O. Auciello, A. Munkholm, C. Thompson, P. H. Fuoss, P. Fini, S. P. DenBaars, and J. S. Speck, *MRS Bull.* **24**, 21 (1999).
- ⁴⁵R.-V. Wang, F. Jiang, D. D. Fong, G. B. Stephenson, P. H. Fuoss, J. A. Eastman, S. K. Streiffer, K. Latifi, and C. Thompson, *Thin Solid Films* **515**, 5593 (2007).
- ⁴⁶M. C. Sullivan, M. J. Ward, A. Gutiérrez-Llorente, E. R. Adler, H. Joress, A. Woll, and J. D. Brock, *Appl. Phys. Lett.* **106**, 031604 (2015).
- ⁴⁷M. Brahlek, A. S. Gupta, J. Lapano, J. Roth, H. T. Zhang, L. Zhang, R. Haislmaier, and R. Engel-Herbert, *Adv. Funct. Mater.* **27**, 1702772 (2017).
- ⁴⁸G. Eres, J. Z. Tischler, M. Yoon, B. C. Larson, C. M. Rouleau, D. H. Lowndes, and P. Zschack, *Appl. Phys. Lett.* **80**, 3379 (2002).